TOWARDS CRUSTAL RESERVOIR FLOW STRUCTURE MODELLING THROUGH INTERACTIVE 3D VISUALIZATION OF MEQ & MT FIELD DATA

John Rugis[1], Peter Leary[1], Marcos Alvarez[1] , Eylon Shalev[1] and Peter Malin[1]

[1] Institute of Earth Science and Engineering, University of Auckland, New Zealand

j.rugis@auckland.ac.nz

Keywords: 3D visualization, scientific data visualization, data modelling, magnetotelluric data, microseismic data, reservoir flow structure.

ABSTRACT

We seek to use modern 3D graphics visualization to enable human visual pattern recognition to assess reservoir structures manifested by in situ fracture systems. In situ flow structures of crustal reservoirs have hitherto been largely assumed to be tied to specific formations and essentially uniform within a given formation. However, neither working assumption has been particularly successful in guiding the drill bit to new active portions of a given geothermal field. A greater degree of in situ spatial flow complexity is hypothesized, and that complexity is almost certainly due to fracture-system control of reservoir fluid pathways.

Four types of geophysical field data have demonstrated a close association with in situ fracture content: micro-seismic event locations, microseismic shear wave splitting density and alignment, magnetotelluric resistivity distributions and magnetotelluric polarization alignment. Visually combining any/all such geophysical field data 3D distributions would help reservoir operators to formulate more rational drilling assessments based on fracture content of the reservoir formations.

To this end, we define the general 3D data visualization problem (Rugis 2008) in an abstract way in which we map either a structured or unstructured finite discrete position mesh into 3D space and then assign scalar and/or vector data values, possibly time varying, to elements of that mesh. In practice, fracture-relevant geophysical data-sets can consist of point data (e.g., microseismic event locations and magnitudes), 2D mesh data (e.g., electrical conductivity data along multiple planar-cut grids) or volumetric data (e.g., tomographic treatments of shear-wave splitting data) and each of these data types can be assigned to an appropriately designed common mesh in a natural way.

We present data treatments using a software toolset of complementary packages within a well-defined data interface to allow ready application to specific reservoir data sets, ultimately including 3D flow modelling. Data sets treated are synthetic microseismic event locations based on spatial correlations observed in geothermal field microseismic data (Section 2); synthetic porosity/fracture-density distributions consistent with observed well-log spatial fluctuation statistics (Section 3); seismic wave speed distributions inferred from geothermal field microseismic event locations (Section 4); the spatial distribution of *in situ* fracture density from observation of seismic shear-wave splitting (Section 5); magnetotelluric survey inversions from forward modelled response curves for synthetic spatial distributions of fracture density fluctuations based on a generic geothermal low resistivity plume (Section 6).

1. INTRODUCTION

Fluid flow in fractured rock is generally understood to be a basic feature of geothermal systems. The observational and intellectual tools to manage flow in geothermal reservoirs are, however, ill-suited to the fundamental spatial complexity of fracture-borne fluid flow.

Existing geothermal reservoir observations and concepts are typically fit to earth models comprising a small range of geologically identified formations that are assumed to have essentially uniform physical properties. Non-uniformity in physical properties is for the most part limited to an assortment of mechanically discontinuous fault structures added to the geological-formation model as needed.

Such reservoir models have a simple but profound defect. If we log a well drilled through the reservoir model we record a series of step-functions in logged properties as the well penetrates the sequence of quasi-uniform reservoir layers and/or faults. The Fourier spectrum of such a numerical log has a specific property explicitly associated with step functions:

$$S(k) \sim 1/k^2, \qquad (1)$$

where k is the spatial frequency and $S(k)$ the property spatial variation power at spatial frequency k.

Unfortunately for the above reservoir model, well-log spectra (1) are rarely if ever observed in nature (Leary 2002). Almost universally, well-log spectra are observed to scale inversely with the first rather than the second power of spatial frequency,

$$S(k) \sim 1/k^1, \qquad (2)$$

where the range of observed spatial frequencies extends over five decades, ~1/km < k < ~1/cm.

We note in passing that well-log power law scaling power spectrum (2) is also distinct from the spectrum of 'white' or 'Gaussian' spatial fluctuations characterized by

$$S(k) \sim 1/k^0 \sim const. \qquad (3)$$

It turns out that, while physical structures characterized by spatial fluctuations associated with spectra (1) or (3) are susceptible to modelling by assumed quasi-uniform physical properties, the physical structure of crustal rock as characterized by spectrum (2) is not effectively approximated by quasi-uniformity and/or spatial averaging. As a result, geophysical processes effectively conditioned by *in situ* fracture spatial heterogeneity need visualization

and conceptual modelling tools that do not depended on quasi-uniformity and/or spatial averages.

Our intent here is to display field or synthetic geophysical data related to *in situ* fracture distributions -- that is, consistent with spatial fluctuations with spatial frequency spectrum (2) -- using software tools designed for visual inspection of complex 3D spatial arrays. Five aspects of geothermal reservoir data are treated in the following sections.

2. MICROSEISMIC EVENT LOCATIONS

Microseismic events occurring either naturally or stimulated by downhole pressurization (e.g., hydrofracturing) are often visibly spatially distributed in clusters, presumably related to the spatial distribution of existing fractures and fracture-networks (Baria & Green 1989; Malin et al. 1989; Stroujkova & Malin 2002; Häring et al. 2008; Kenedi et al. 2010). We know from (2) that such clusters are likely to occur on scale lengths from meters to kilometres. The question becomes: what tools do we have to visually identify spatial clustering in microseismic data and how can we use that clustering information to better model a reservoir?

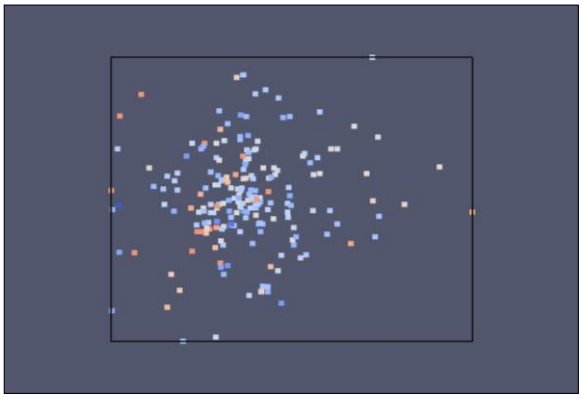

Figure 1: Seismic event locations: scatter plot.

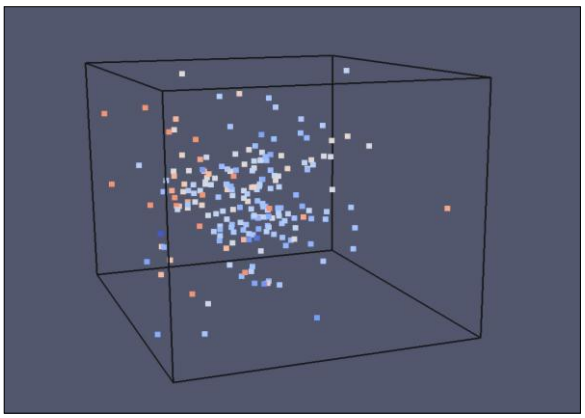

Figure 2: Seismic event locations: 3D scatter plot.

2.1 Event location and magnitude

Perhaps the simplest visual representation consists of an orthogonal projection scatter plot with color-coded magnitude as shown in Figure 1. An arbitrary rotation projection (e.g., Foley 2002) scatter plot with bounding box as shown in Figure 2 conveys some idea of the 3D spatial distribution of events. Keep in mind that such arbitrary rotations can be implemented in real-time under user control while viewed on a computer screen.

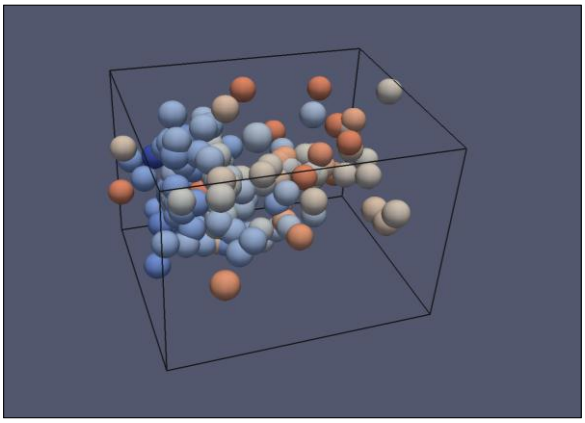

Figure 3: Seismic event locations: spherical glyphs..

As shown in Figure 3, 3D spatial location visualization can be enhanced through the use of suggestive “glyphs”, in this example, spheres.

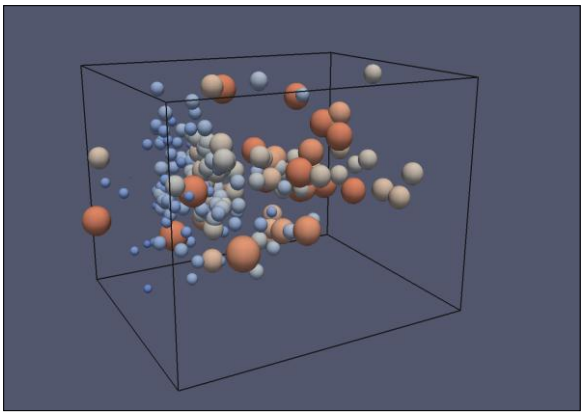

Figure 4: Seismic events: location and magnitude.

An additional enhancement, as shown in Figure 4, uses sphere glyph size to re-enforce the indication of magnitude.

3. FRACTURE AND POROSITY DISTRIBUTIONS

Neutron porosity well-logs are good examples of well-log spatial fluctuation data whose spectra scale as (2) (Leary & Malin 2008a,b). In a parallel data set, clastic reservoir well-core sequences indicate that spatial variations in well-core porosity control well-core permeability through fracture-connectivity (Leary & Walter 2008). The effective ‘poroperm’ fluctuation relation is

$$\delta\varphi \sim \delta\log(\kappa) \qquad (4)$$

where $\delta\varphi$ is a zero-mean/unit-variance sequence of well-core porosities, and $\delta\log(\kappa)$ is a zero-mean/unit-variance sequence of the logarithm of well-core permeability. Knowing that neutron porosity obeys (2), we can visualize through poroperm relation $\delta\varphi \sim \delta\log(\kappa)$ how permeability varies in space. This will help understand spatially complex fluid flow in a reservoir.

3.1 Modelling fractures and faults

3D scientific modelling often produces volumetric data cubes (e.g., Klette & Rosenfeld 2004) which are difficult to visualize because the cells within internal regions of the cube are obscured. Figure 5 shows a 128x128x128 synthetic porosity data cube which models both depth effects and a vertical fracture zone. Visualization software subset extraction tools can be used to reveal otherwise obscured data such as the extracted fault slab shown in Figure 6. Subset extraction tools can also be applied at the cell level to produce images such as Figure 7 in which cells with porosity below a threshold have been removed.

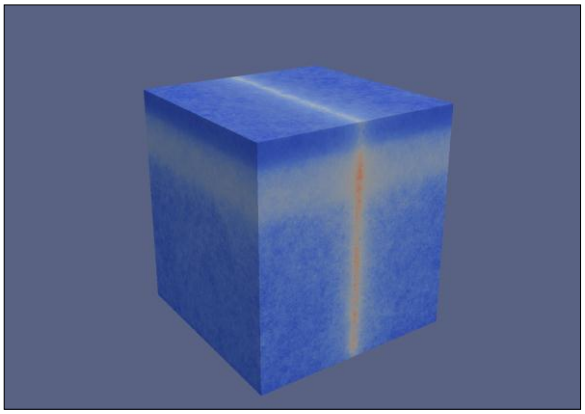

Figure 5: Synthetic porosity: depth-layers and fault.

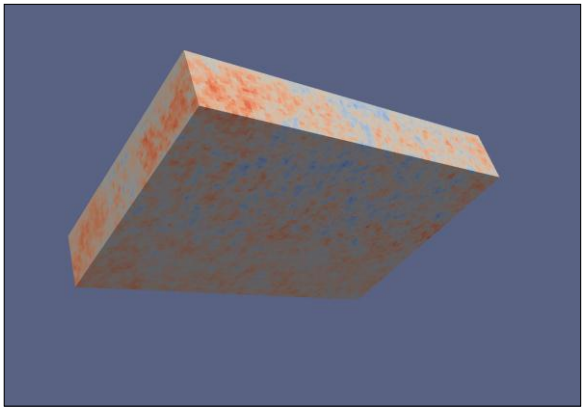

Figure 6: Synthetic porosity: extracted fault slab.

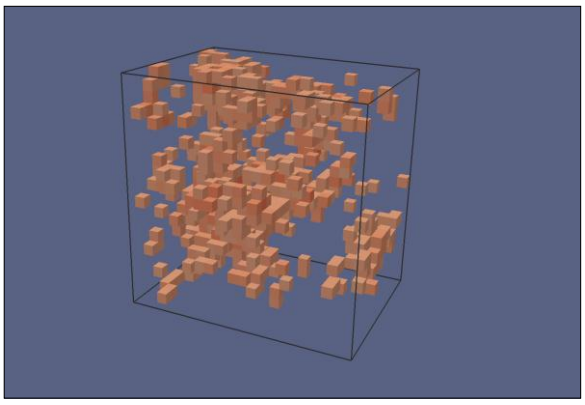

Figure 7: High porosity cells extracted from fault slab.

3.2 Modelling porosity

Data cube subset extraction and high porosity cell elimination can be used to produce images which are suggestive of open flow channels. Figure 8 shows an orthogonal projection of an extracted porosity slab in which the flow channels are represented as voids. The rotation projection shown in Figure 9 is more representative of the real-world in that it reveals additional less direct flow paths. So far, all of the individual data cells have been shown as small cubes which can give a false impression of stepped surface area. Figure 10 shows the same data-set rendered for display with an algorithm that more accurately represents surface area.

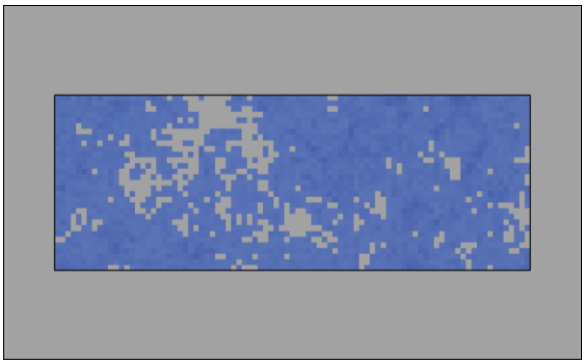

Figure 8: Extracted slab of low porosity cells.

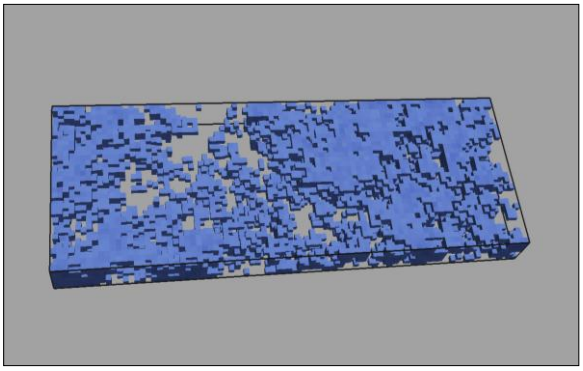

Figure 9: 3D view of low porosity cells.

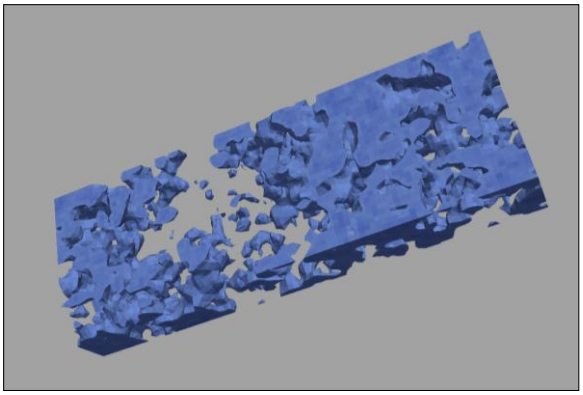

Figure 10: Surface rendering of low porosity cells.

4. SEISMIC WAVE SPEED DISTRIBUTIONS

Microseismic event location involves simultaneous solution to "where is an event in space", and "what is the velocity structure" of the host reservoir that effects the putative event location (Kenedi et al. 2010). This is far from a straightforward inversion process, and it is important to be able to visualize how event clusters may be developing. Is, for instance, the cluster real or an artefact of the inversion process? In the inversion process, it is useful to be able quickly inspect event clustering, perhaps to identify cluster events by waveform similarity/coherence.

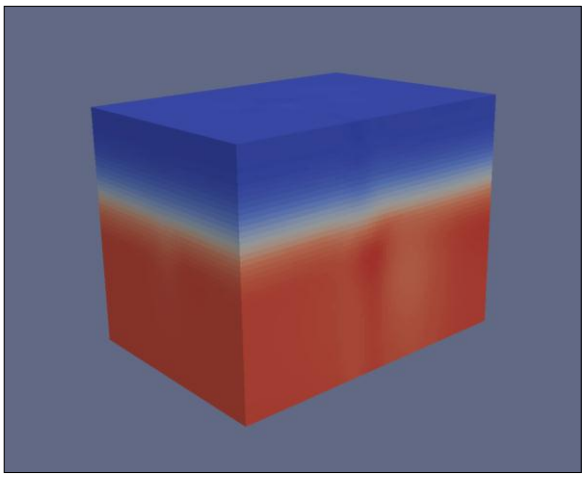

Figure 11: Pressure-wave velocity data cube.

Figure 11 shows a 70x50x50 pressure-wave velocity data cube which has been computed from geothermal field microseismic measurements (e.g., Ropinski 2005). As was the case with the full data cube in the previous section, internal regions are obscured.

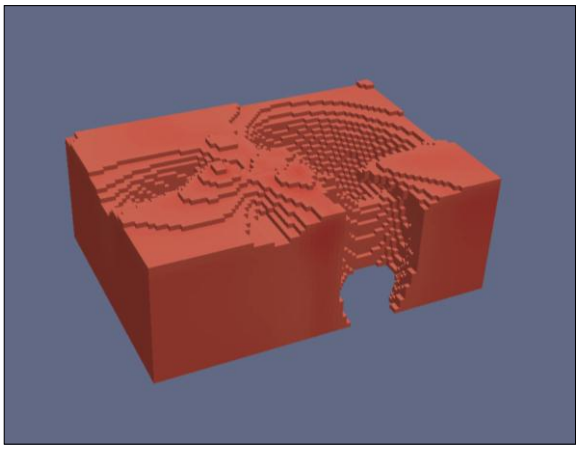

Figure 12: Extracted high-pass velocity.

4.1 Visualizing velocity data: Method 1

The data cells in low velocity regions have been carved away in Figure 12. A smooth surface rendering of the same remaining cells is shown in Figure 13. The smoothed rendering not only more accurately represents the equal valued surface area, it also reveals more surface contour detail.

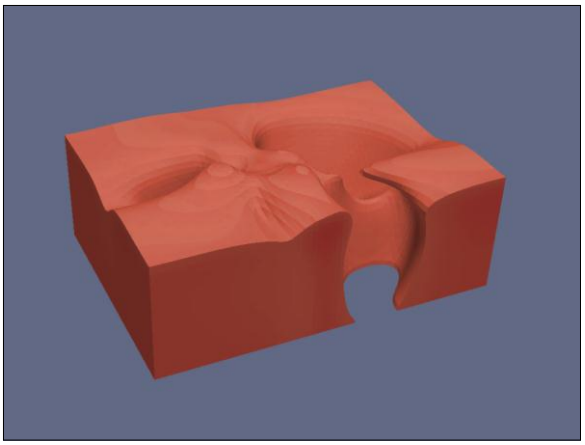

Figure 13: Smooth rendering of high-pass velocity.

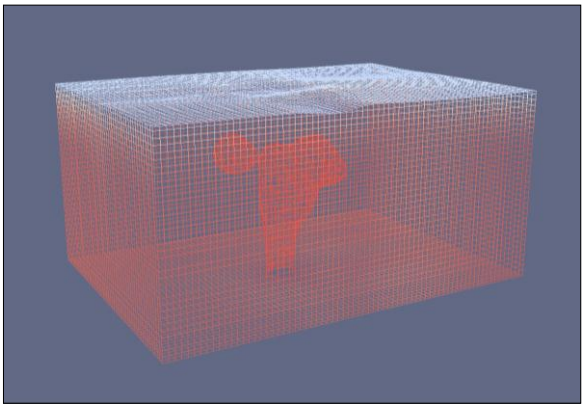

Figure 14: Wire-frame view of band-pass velocity.

In an attempt to reveal internal structure, the associated so-called wire-frame view in Figure 14 reveals the presence of an internal high velocity region.

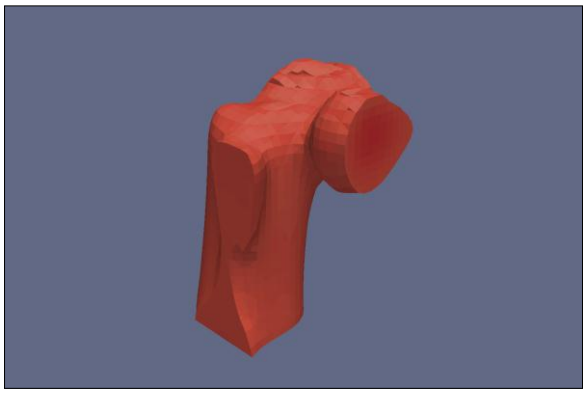

Figure 15: Extracted high-pass velocity.

The result of a subsequent even higher high-pass velocity extraction is shown in Figure 15. Keep in mind that all of the images in this report have been created in an interactive exploratory computer environment in which one result often suggests another.

4.2 Visualizing velocity data: Method 2

More recent advances in computer graphics technology have opened up the possibility of real-time interactive volumetric rendering (e.g., Hadwiger 2009). Volumetric rendering makes extensive use of glass-like transparency models and sophisticated illumination lighting effects which enable selective "seeing through" data.

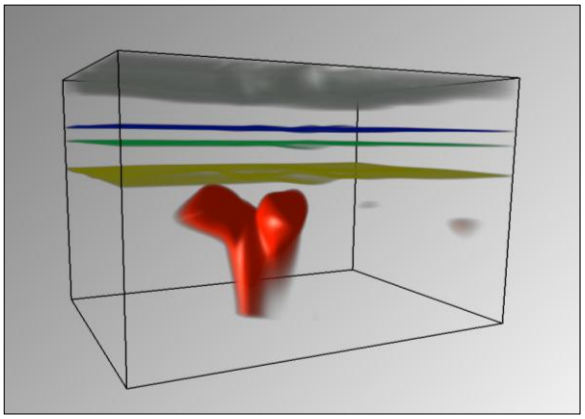

Figure 16: Pressure-wave velocity.

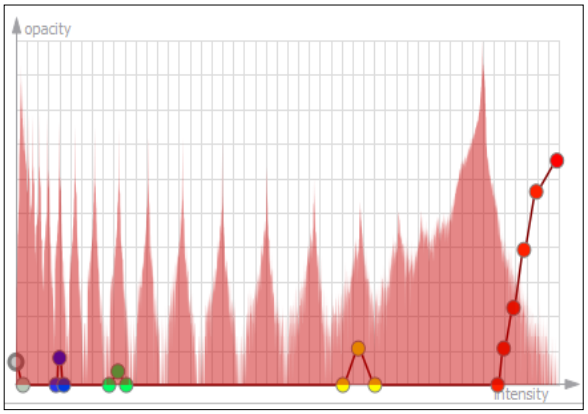

Figure 17: Pressure-wave velocity transfer function.

Figure 16 shows a volumetric rendering of the same pressure-wave data-set generated using a user specified visual data transfer function. The visual transfer function is shown in Figure 17. The graph in Figure 17 contains a histogram of the velocity data in the background as well as a display colour mapping curve in the foreground. The display colour mapping curve offers the user four degrees of freedom in colour specification: hue, saturation, lightness and transparency. Note that four of the spikes in the histogram have been assigned distinct colours (grey, blue, green, yellow) and that these data spikes are associated with depth layers as seen in Figure 16. Roughly the same high velocity region previously shown in the previous sub-section is once again highlighted in red.

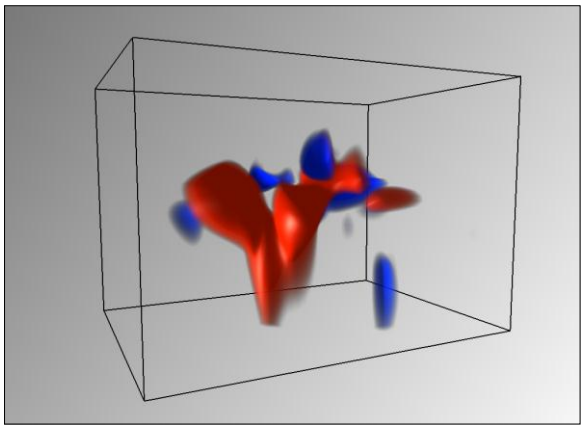

Figure 18: Depth normalised pressure-wave velocity.

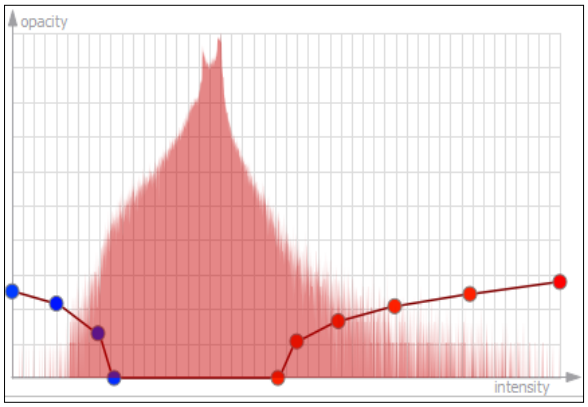

Figure 19: Depth normalised velocity transfer function.

The histogram spikes in Figure 17 along with the rendering in Figure 16 illustrate the presence of a distinct depth layering in velocity distribution. In Figures 17 and 18 the underlying data has been depth normalized to better reveal non depth related local velocity anomalies. Note that the highest and lowest velocity regions do not extend to the surface.

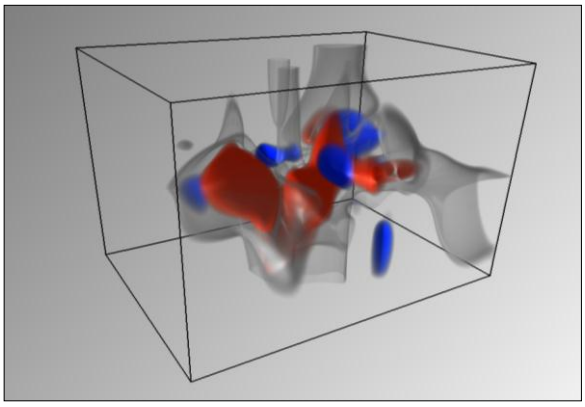

Figure 20: Depth normalised pressure-wave velocity.

In an attempt to discover which velocities do in fact reach the surface, an additional histogram range was marked to be displayed in grey colour, as shown in Figure 21, with the result shown in Figure 20.

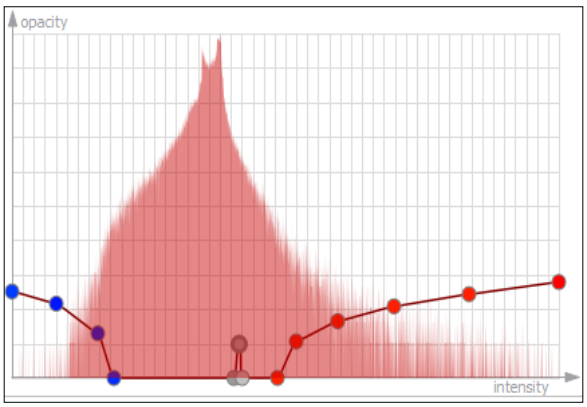

Figure 21: Adjusted velocity transfer function.

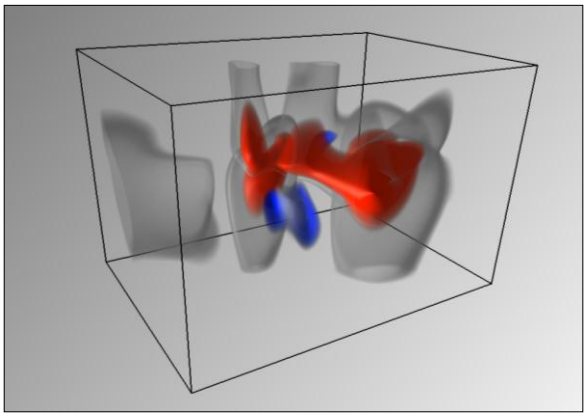

Figure 22: Depth normalised shear-wave velocity.

And finally, in this section, the same velocity transfer function has been used in the display of shear-wave velocity computed from the same initial microseismic data-set.

5. FRACTURE DENSITY DISTRIBUTION

Seismic shear-waves traveling upwards to the earth's surface often encounter crustal volumes of stress-aligned microfractures, and as a result 'split' into a faster wave polarization parallel to the fracture alignment, and a slower wave polarization normal to the fracture alignment. The direction and degree of 'shear-wave splitting' is a powerful diagnostic of *in situ* fracture density distribution (Lou & Malin 1997; Kenedi et al. 2010).

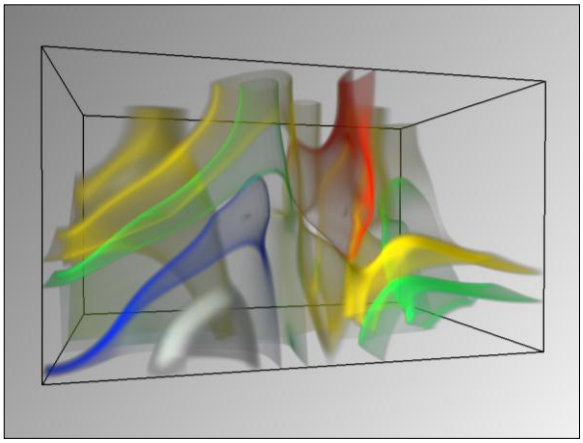

Figure 23: Fracture density.

A full range of colours, from red to yellow through to blue and grey, have been used to illustrate a fracture density distribution (generated from microseismic field data) as shown in Figure 23. In this case, the highest crack density reaches the surface and a "bump" of low crack density is submerged.

6. MAGNETOTELLURIC RESISTIVITY DISTRIBUTION

The same fracture alignment that induces shear-wave splitting can also induce differences in the magnitude of nature electromagnetic (EM) currents flow along the fracture direction and across the fracture direction (Leary et al. 2010). As *in situ* fracture distributions are neither vertically or horizontally homogeneous in space, it is desirable to model/interpret the EM response of the earth in terms of spatially heterogeneous fracture distributions. The EM response to a heterogeneous distribution of *in situ* fractures is, however, far more complex than that usually allowed for in EM modelling. We compute a sequence of 2D EM response curves for vertical planes through a spatially complex 3D fracture distribution, and display the resulting inversion sections in terms of a pseudo-3D conductivity/ fracture-density volume. Two *in situ* fracture structures are targeted – a vertical fault, and a vertical conductivity silo routinely associated with geothermal outcrops (Bibby et al 1995).

6.1 Vertical fault model

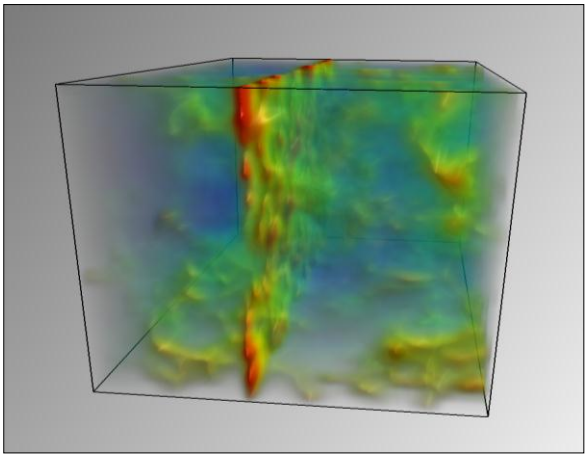

Figure 24: Synthetic conductivity: fault.

Figure 24 shows the results of 128x128x29 model of conductivity through a vertical fault region. (Note that with full 3D MT surveys there is generally a reduced resolution in one direction.) A full range of colours, from red to yellow through to blue and purple, have been used with red representing the highest conductivity. The visually obvious spatial variations in conductivity are very suggestive of the complexities likely to be found in the real-world.

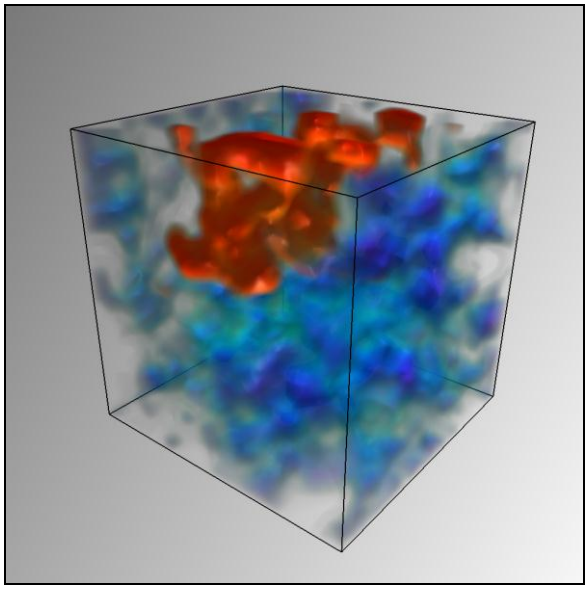

Figure 25: Synthetic conductivity: thermal outcrop.

6.2 Vertical conductivity silo

A 128x128x24 model of a vertical cylindrical conductivity silo extending down from the surface, as is routinely associated with a geothermal outcrop, is shown in Figure 25. Once again, the modelled spatial variations in conductivity are suggestive of the complexities likely to be found in the real-world

7. CONCLUSION

These exercises in 3D data visualization should be seen as the start of a larger program of merging different geophysical data sets into a larger 3D visualization scheme. Grant (2009) documents how inefficient and unpredictable are well siting and well productivity in geothermal reservoirs. Ideally, and potentially practically, geothermal well siting inefficiency/unpredictability can be reduced by acquiring data on microseismic event locations, seismic velocity structures, shear wave splitting, and EM response curves that can be jointly visualized. Joint visualisation sets the stage for a joint data inversion for two or three physical aspects of the *in situ* fracture distributions that control the complex flow structures of geothermal reservoirs.

ACKNOWLEDGEMENTS

The authors would like to credit the University of Münster and Linköping University for their open-source software volumetric rendering engine, Voreen. We would also like to credit Kitware, Sandia National Labs and CSimSoft for their open-source data analysis and visualization application, Paraview.

REFERENCES

Baria, R. and A. S. P. Green.. "Microseismics: A Key to Understanding Reservoir Growth." In *Hot Dry Rock Geothermal Energy, Proc. Camborne School of Mines International Hot Dry Rock Conference*, Ed. Roy Baria, Camborne School of Mines Redruth, Robertson Scientific Publications, London, pp. 363-377 (1989).

Bibby, H.M., Caldwell, T.G., Davey, F.J., and Webb, T.H. Geophysical evidence on the structure of the Taupo Volcanic Zone and its hydrothermal circulation, *J Volcanology and Geothermal Research* 68, 29-58 (1995).

Foley, J. D., van Dam, A., Feiner, S. K. and Hughes, J. F.: *Computer Graphics: Principles and Practice*. Addison-Wesley, Boston. (2002).

Grant, M.A. Optimisation of drilling acceptance criteria, *Geothermics* 38, 247-253 (2009).

Hadwiger, M., Ljung, P., Rezk Salama, C. and Ropinski, T.: Advanced Illumination Techniques for GPU-Based Volume Ray-Casting. *Proc. Course at Eurographics*. pp. 39 – 212. (2009).

Häring, M.O., U. Schanz, F. Ladner, B.C. Dyer, Characterisation of the Basel 1 enhanced geothermal system, *Geothermics* 37, 469,495 (2008).

Kenedi, C.L., E. Shalev, A. Lucas, and P. Malin, Microseismicity and 3-D Mapping of an Active Geothermal Field, Kilauea Lower East Rift Zone, Puna, Hawaii, *Proceedings World Geothermal Congress* Bali, Indonesia (2010).

Klette, R. and Rosenfeld, A.: *Digital Geometry*. Morgan Kaufmann, San Francisco. (2004).

Leary P., P. Malin, E. Shalev & S. Onacha Aquifer heterogeneity – is it properly assessed by wellbore samples and does it matter for aquifer heat extraction? *Proccedings Australian Geothermal Conference*, Adelaide, 16-19 November (2010).

Leary, P.C. and Malin P.E. Advection Heat Flow and the 1/F-Noise Fracture Nature of Crustal Rock, *Proceedings Australian Geothermal Energy Conference*, Melbourne, 19-22 August (2008a).

Leary P & Malin P Thermal-gradient & porosity well-log fluctuation relation as guide to *in situ* advective flow structure, *Proceedings of the 30th New Zealand Geothermal Workshop*, Taupo, New Zealand, 11-13 November (2008b).

Leary, P.C. Fractures and Physical Heterogeneity in Crustal Rock, In: J.A. Goff & K. Holliger (eds.) *Heterogeneity of the Crust and Upper Mantle – Nature, Scaling and Seismic Properties*, Kluwer Academic/Plenum Publishers, New York, 155-186 (2002).

Leary, P.C. & Walter, L.A. Crosswell seismic applications to highly heterogeneous tight-gas reservoirs, *First Break* 26, 49-55 (2008).

Lou, M., E. Shalev, and P.E. Malin, Shear-wave splitting and fracture alignments at the northwest Geysers, California, *Geophys. Res. Lett*. 24, 1895-1898 (1997).

Malin, P.E., S.N. Blakeslee, M.G. Alvarez, and A.J. Martin Microearthquake imaging of the Parkfield asperity, *Science* 244: 557–559 (1989).

Ropinski, T. and Hinrichs, K.: Interactive Volume Visualization Techniques for Subsurface Data. *Proc. International Conference on Visual Information Systems*, pp. 121 – 131. (2005).

Rugis, J.: *Digital Surface Curvature – Identifying and Visualizing Surface Detail*. VDM Verlag, Saarbrücken. (2008).

Stroujkova, A.F. and P.E. Malin. Multiple ruptures for Long Valley microearthquakes: A link to volcanic tremor, *J Volcanology and Geothermal Research*, 106, 123-143 (2002).